Astron. Astrophys. 232, 277–291 (1990)

ASTRONOMY AND ASTROPHYSICS

3-D simulation of turbulent cyclonic magneto-convection

A. Brandenburg[1], Å. Nordlund[2], P. Pulkkinen[3], R. F. Stein[4], and I. Tuominen[1]

[1] Observatory and Astrophysics Laboratory, University of Helsinki, Tähtitorninmäki, SF-00130 Helsinki, Finland
[2] Copenhagen University Observatory, Øster Voldgade 3, DK-1350 Copenhagen K, Denmark
[3] Department of Theoretical Physics, University of Helsinki, Siltavuorenpenger 20 C, SF-00170 Helsinki, Finland
[4] Department of Physics and Astronomy, Michigan State University, East Lancing, Michigan 48824-1116, USA

Received September 4; accepted December 19, 1989

Abstract. We present results of simulating turbulent three-dimensional magneto-convection under the influence of rotation for a layer whose depth is about one pressure scale height. The fluid is assumed to be a compressible conducting perfect gas. The axis of rotation and the direction of gravity are parallel and oriented downwards. That is, our model may be compared with a location at the southern pole of the Sun. For 300 times supercritical Rayleigh numbers irregular variations of the magnetic field and velocity pattern occur on a time scale comparable with the rotation period (which corresponds to about five turnover times and about two Alfvén times). We find a systematic separation of positive and negative kinetic helicity, $\langle \boldsymbol{\omega}' \cdot \boldsymbol{u}' \rangle$ (with $\boldsymbol{\omega}' = \mathrm{curl}\, \boldsymbol{u}'$), in the upper and lower layers of the model, which is obviously due to the influence of rotation. Magnetic helicity, $\langle \boldsymbol{J}' \cdot \boldsymbol{B}' \rangle$, has a similar variation with depth, but the sign is opposite to that of the kinetic helicity. The mean electromotive force $\langle \boldsymbol{u}' \times \boldsymbol{B}' \rangle$ is directed downwards in the upper layers and upwards in the lower layers, whilst the mean magnetic field $\langle \boldsymbol{B} \rangle$ is mainly directed downwards. This may be described by an α-effect with $\langle \boldsymbol{u}' \times \boldsymbol{B}' \rangle = \alpha \langle \boldsymbol{B} \rangle$, where α is positive in the upper part and negative in the lower part. α determined in this way is roughly equal to $0.1\tau \langle \boldsymbol{\omega}' \cdot \boldsymbol{u}' \rangle$, where τ is the correlation time. Traditional results for the α-effect in mean-field dynamo theory give a negative proportionality to the kinetic helicity. We argue that the positive proportionality found from the simulations is a topological consequence of the particular way field lines are being twisted by the flow.

Key words: stellar convection – turbulence – magnetic field topology – mean-field dynamo – the Sun: magnetic fields

1. Introduction

The hydrodynamics of stellar convection zones is still very poorly understood. One reason is that the Rayleigh and Reynolds numbers in these regions are extremely high, and are far from being accessible by laboratory experiments or numerical simulations. Order-of-magnitude estimates and coarse numerical simulations are the only practicable approaches for the computation of stellar models. It may appear surprising that standard mixing length models give satisfactory results for many stars by adjusting a single parameter, which, in addition, turns out to be close to unity. However, as shown by Gough & Weiss (1976), the only important effect of the mixing length parameter in envelope models is to determine the entropy jump, which occurs in a very thin layer close to the surface for non-giant stars. Models calculated with different formulations of the mixing length estimates, but calibrated to a given radius and luminosity, have practically the same entropy jumps, and only the detailed structure of the thin superadiabatic layer differs.

Less success is achieved when the mixing length concept is employed in dynamo theory. Mixing length estimates for the turbulent magnetic diffusivity η_t and, in particular, for the strength of the α-effect (Steenbeck et al., 1966), give results which are several orders of magnitude larger than what is needed for traditional kinematic $\alpha\Omega$-dynamos to produce the 22-year magnetic cycle period of the Sun. It is possible to obtain realistic models for the solar cycle, with the observed large-scale field geometry and migration properties, but α and η_t have to be reduced by factors of about 200 and 10, respectively, compared to mixing length estimates (Brandenburg and Tuominen, 1988). The question is whether this discrepancy is really only a matter of appropriate scaling factors, or whether the underlying physics is seriously misunderstood.

Self-consistent stellar dynamo models have been computed by Gilman and Miller (1981), Gilman (1983), Glatzmaier (1985) and others. They find generation of global magnetic fields and a generation of differential rotation with a *positive* radial gradient ($\partial\Omega/\partial r > 0$), which results in toroidal magnetic field belts migrating towards the poles. rather than towards the equator as in the Sun. These models have angular velocities which are nearly constant on cylindrical surfaces (cf. the Taylor-Proudman theorem), which seems to be inconsistent with the increasingly accurate measurements of the internal rotation of the Sun (cf. Libbrecht, 1988, and other papers in the same proceedings). A possible reason for this discrepancy may be the insufficient resolution of the small scales in the models (cf. Nordlund, 1985). The smallest horizontal scale resolved by Gilman (1983) and Glatzmaier (1985) is about 100 Mm, which is the scale of giant cells. Near the solar surface, most of the convective flux is carried by motions on the scale of a few Mm, with larger scale motions

Send offprint requests to: A. Brandenburg

from deeper layers superimposed. The dominant feature of these motions are isolated, fast, filamentary, and twisting downdrafts that merge into successively larger scale downdrafts with depth (Stein & Nordlund, 1989). To describe motions on such scales in models of the global convection zone is presently not possible. To address these major problems of dynamo theory using *ab initio* computer simulations is a formidable task, that may not be achievable for a number of years.

On the other hand, mean-field models for the dynamo and the differential rotation would provide a powerful approach, if only the theory of the turbulent transport coefficients could be relied upon. For example, analytical models for the small-scale turbulent motions by Rüdiger (1980) give expressions for the Reynolds stresses which may lead to a negative radial gradient of Ω and also to equatorwards migrating toroidal field belts. Furthermore the contours of constant angular velocity are no longer cylindrical, but may be "disk-shaped", when higher order parameters are included (Tuominen & Rüdiger, 1989; Rüdiger, 1989).

Turbulent transport coefficients (like turbulent diffusivity and the α-effect) describe the dependence of certain correlation functions on the mean magnetic field, the mean velocity, and other quantities. The question is, whether it is possible to determine these coefficients by means of direct computer simulations of convection in a small test domain, which is thus considered to represent the conditions in a part of a stellar convection zone. This is not a simple task, and it may even be an impossible one. The situation is similar to the problem of subgrid-scale modeling in codes for solving the Navier-Stokes equations. Due to the nonlinear terms, energy is transferred towards smaller and smaller scales continuing down to the dissipation length. If this scale is not resolved by the code, kinetic energy accumulates in the smallest scales resolved. To avoid this, one may either simply use enhanced molecular viscosities, introduce a flow-dependent turbulent viscosity, or else resort to numerical methods that directly prevent accumulation of too much kinetic energy in the smallest scales. The question is how applicable such methods are in MHD cases. Here we use an enhanced molecular viscosity, because it leads to a well posed problem, and quantitative comparisons with previous work can be made.

We expect that turbulent diffusivities and other mean-field transport coefficients should, in some sense, always be related to the scale on which they are used. For example, a model with 100 gridpoints in one direction is limited to a Reynolds number of about 100, if we restrict ourselves to a maximal grid Reynolds number of about unity. Similarly, the Taylor number should not exceed a value of about 100^2. For a model with solar rotation rate $\Omega = 3 \times 10^{-6}\mathrm{s}^{-1}$ and an extension of, e.g., $d = 100\,\mathrm{Mm}$ the "effective viscosity" (corresponding to $\mathrm{Ta} = 10^4$) is $2\mathrm{Ta}^{-1/2}\Omega d^2 \approx 5 \times 10^{12}\mathrm{cm}^2/\mathrm{s}$. The turbulent viscosity in the Sun is expected to be anisotropic on large scales (cf. Kippenhahn, 1963). The strength and direction of such anisotropies depend on the rotation rate and the properties of the turbulence and may be obtained, in principle, from computer simulations. We anticipate that on sufficiently small scales the effective viscosity is approximately isotropic and may then be replaced by the expressions valid for the molecular viscosity.

Mean-field transport coefficients, such as the α-effect, have often been derived from simple MHD-flows which arise from various linear instabilities (e.g. Soward, 1979; Brestenský & Rädler, 1989). On the other hand it is also possible to compute directly magnetic field generation and dynamo action as a result of convective motions (Childress & Soward, 1972; Fautrelle & Childress, 1982). Recently, Meneguzzi and Pouquet (1989) investigated turbulent convective dynamo action by means of direct 3-D simulations in a shallow layer of incompressible fluid with and without rotation. Our present work is related to that of Meneguzzi and Pouquet. The main differences are that we allow the fluid to be compressible and we assume a vanishing horizontal magnetic field at the boundaries. We take an initially vertical homogeneous magnetic field, rather than only a weak seed-field, as in the computations of Meneguzzi and Pouquet, because we are here mainly interested in deriving an α-effect rather than simulating a self-excited dynamo. Here, in contrast to the cases studied by Meneguzzi and Pouquet, rotation seems to play an important role, because it leads to a systematic separation of regions with positive and negative helicities, which is important for the α-effect.

This paper is arranged as follows: in Sect. 2 we review the basic equations and boundary conditions defining the mathematical problem. We then describe various 2-D test calculations and comparisons with previous results by Hurlburt et al. (1984) and Hurlburt & Toomre (1988). In Sect. 4 we describe the results of our 3-D runs and discuss the relevance for α-effect dynamos in Sect. 5. In the last section we give the conclusions.

2. The model

We consider a fully compressible fluid heated from below taking the dynamical effects of magnetic fields and rotation into account. We are interested in the lower layers of the convection zone and we may therefore neglect radiation. On the other hand, we need the presence of heat conduction and viscosity in order to keep the Rayleigh number finite. We take *constant* coefficients $\mathscr{K}$ and μ for heat conduction and shear viscosity, which allows direct comparisons with previous models by Hurlburt and Toomre (1988). However, this leads to a strong variation of the local Rayleigh number with height, and it may be more reasonable to instead treat the kinematic viscosity $\nu \equiv \mu/\rho$ as a constant (and similarly $\kappa \equiv \mathscr{K}/\gamma\rho$). For the present runs, which cover only one scale height, the variation of the local Rayleigh number with height is perhaps not so critical.

We assume all variables to be periodic in the horizontal direction. This is numerically convenient and avoids artificial boundaries. However, it is then impossible to include the centrifugal force in the momentum equation. In some of the cases considered below this approximation may not be strictly justifiable as the centrifugal force may not be small compared to other *horizontal* forces. (It is, of course, always negligible compared to gravity.) However, we do not feel that this neglect influences our general results about the nature of the turbulent motions.

2.1. Basic equations

We solve the equations for conservation of mass, momentum, energy, and the induction equation in the form

$$\frac{\mathrm{D}\ln\rho}{\mathrm{D}t} + \mathrm{div}\,\boldsymbol{u} = 0, \tag{1}$$

$$\frac{\mathrm{D}\boldsymbol{u}}{\mathrm{D}t} = -\frac{p}{\rho}\nabla\ln p + \boldsymbol{g} - 2\boldsymbol{\Omega}\times\boldsymbol{u} + \frac{1}{\rho}\boldsymbol{J}\times\boldsymbol{B} + \frac{1}{\rho}\mathrm{Div}\,\boldsymbol{\tau}, \tag{2}$$

$$\frac{De}{Dt} = -\frac{p}{\rho}\,\mathrm{div}\,\boldsymbol{u} + \frac{\mathscr{K}}{\rho}\nabla^2 e + Q_{\mathrm{visc}} + Q_{\mathrm{Joule}}, \tag{3}$$

$$\frac{\partial \boldsymbol{B}}{\partial t} = \mathrm{curl}\,(\boldsymbol{u}\times\boldsymbol{B} - \boldsymbol{J}/\sigma), \tag{4}$$

where e is the specific internal energy of the gas which we assume to be ideal, i.e. $p/\rho = (\gamma-1)e$, where γ is the ratio of the specific heats c_p and c_v, respectively. (c_p and c_v are assumed to be constant.) In the following we assume $\gamma = 5/3$.

The stress tensor $\boldsymbol{\tau}$ is

$$\tau_{ij} = \mu(u_{i,j} + u_{j,i} - \tfrac{2}{3}\delta_{ij}\mathrm{div}\,\boldsymbol{u}), \tag{5}$$

where commas denote derivatives and index 3 refers to the z-direction. In the case of constant μ we simply have

$$\mathrm{Div}\,\boldsymbol{\tau} = \mu(\nabla^2\boldsymbol{u} + \tfrac{1}{3}\mathrm{grad}\,\mathrm{div}\,\boldsymbol{u}). \tag{6}$$

Q_{visc} is the rate of viscous heating

$$Q_{\mathrm{visc}} = \tau_{ij}u_{i,j}/\rho, \tag{7}$$

which is given explicitly by

$$\begin{aligned} Q_{\mathrm{visc}} = &\frac{\mu}{\rho}\,[(u_{1,2}+u_{2,1})^2 + (u_{2,3}+u_{3,2})^2 + (u_{3,1}+u_{1,3})^2 \\ &+ 2(u_{1,1}^2 + u_{2,2}^2 + u_{3,3}^2) - \tfrac{2}{3}(\mathrm{div}\,\boldsymbol{u})^2]. \end{aligned} \tag{8}$$

$Q_{\mathrm{Joule}} = \boldsymbol{J}^2/\rho\sigma$ is the rate of Joule heating per unit mass, where $\boldsymbol{J} = \mathrm{curl}\,\boldsymbol{B}/\mu_0$ is the electric current and σ the electric conductivity. The condition $\mathrm{div}\,\boldsymbol{B} = 0$ has to be satisfied by the initial field.

2.2. The initial and boundary conditions

For reasons of comparison we have computed all our models with the same boundary conditions as Hurlburt and Toomre (1988). The initial mean state is a polytropic stratification with the polytropic index $m = 1$ and a constant, vertically oriented magnetic field B_0. The initial profiles for ρ and e are given by

$$\rho = \rho_0(z/z_0)^m, \quad \text{and} \quad e = gz/[(\gamma-1)(m+1)], \tag{9}$$

where ρ_0 is the initial density at the top layer $z = z_0$. The initial state is then specified by ρ_0 and g. The vertical coordinate z increases downwards. The degree of stratification is parameterized by the density contrast $\chi \equiv \rho(z_0+d)/\rho(z_0) = (1+d/z_0)^m$. The number of pressure scale heights covered by the model is then $n_p \equiv \Delta\ln p = \Gamma\ln\chi$, where $\Gamma = (m+1)/m$.

As the thermal boundary condition we keep the temperature on the top layer constant and prescribe the vertical gradient of e on the bottom, i.e.

$$\begin{aligned} e &= gz_0/[(\gamma-1)(m+1)] \quad \text{on} \quad z = z_0, \\ de/dz &= g/[(\gamma-1)(m+1)] \quad \text{on} \quad z = z_0 + d. \end{aligned} \tag{10}$$

In order to facilitate comparison with Hurlburt and Toomre we choose $\rho_0 = 1$ and $g/[(\gamma-1)(m+1)] = 1$. We take the depth of the layer $d = 1$, which automatically determines the time unit to be $[(\gamma-1)(m+1)d/g]^{1/2}$. This is related to the sound travel time across the layer, $\int dz/c$, which is $2(\chi^{1/2m}-1)[\gamma(\gamma-1)(\chi^{1/m}-1)]^{-1/2}$ in these units (e.g. 0.79 for $\chi = 2$ and 1.39 for $\chi = 11$). Here, c is the adiabatic speed of sound with $c^2 = \gamma(\gamma-1)e$. In the following we shall refer sometimes to "sound travel time" and mean by that the time unit as defined above.

The initial velocity field consists of a combination of a cellular flow and a random perturbation. We exclude penetration and require the horizontal components of viscous and magnetic stress to vanish at both boundaries, i.e.

$$\left.\begin{aligned} u_{1,3} = u_{2,3} = u_3 = 0 \\ B_1 = B_2 = 0 \end{aligned}\right\} \quad \text{at} \quad z = z_0, z_0 + d. \tag{11}$$

From $\mathrm{div}\,\boldsymbol{B} = 0$ it follows that $B_{3,3} = 0$ at $z = z_0, z_0 + d$. Such closed boundary conditions are perhaps not quite adequate for simulating a "test volume" in the convection zone but it is difficult to formulate physically correct open conditions for MHD-flows. We feel that it may be more important to consider these simulations as a well posed problem, rather than as a "toy box".

2.3. The numerical method

We solve the equations (1)-(4) numerically, using a modification of the code by Nordlund and Stein (1989), which employs a second order Adams-Bashforth time advance and spatial derivatives calculated from cubic splines. Since the density can vary substantially over the layer it is convenient to use $\ln\rho$ instead of ρ as one dependent variable. The other dependent variables are $\boldsymbol{u}$, e, and $\boldsymbol{B}$. We use a Cartesian (x, y, z) coordinate system, where z increases downwards. $\boldsymbol{\Omega}$ is also directed downwards, which corresponds to the situation at the southern pole of the Sun. A uniform z-mesh is used for simplicity. The time step is constantly adjusted to approximately 20% of the Courant time.

The main differences from previous calculations by Nordlund and Stein are the following: their artificial diffusion is replaced by the expressions for molecular viscosity and heat conduction; their penetrating boundaries are changed into impenetrable boundaries; radiation transfer is neglected; and the equation of state is that of a perfect gas. Instead of assuming *natural* splines (vanishing second derivative on the boundaries), we use a spline boundary condition for the first derivative, which is computed from a third order one-sided derivative. A fiducial upper layer (Stein et al., 1989) is not present.

Most of the calculations were carried out on the CRAY XMP-14 and on the CRAY XMP-EA/432 of the National Computing Center of Finland. For a resolution of $31 \times 31 \times 63$ gridpoints the code needs, in the present form, approximately 0.8 sec of CPU time per time step and approximately 1.6 Mwords of memory. About 480 time steps are necessary to cover one sound travel time.

2.4. Horizontal averages

In the following we shall often refer to horizontal mean values which we define as

$$\langle f\rangle = \int dx\,dy\, f \Big/ \int dx\,dy, \tag{12}$$

where the integration is taken over the whole $x-y$ domain. This definition of the averages implies that the Reynolds rules hold. All differential operators commute with the averaging operator and the average of x and y derivatives vanish, i.e.

$$\langle \partial f/\partial x\rangle = \partial\langle f\rangle/\partial x = 0,$$
$$\langle \partial f/\partial y\rangle = \partial\langle f\rangle/\partial y = 0, \quad (13)$$
$$\langle \partial f/\partial z\rangle = \partial\langle f\rangle/\partial z.$$

Since $\mathrm{div}\,\langle \boldsymbol{B}\rangle = \mathrm{div}\,\boldsymbol{B} = 0$, these equations immediately imply that $\langle B_z\rangle$ is independent of z. With reference to the induction equation (4) we note that $\partial\langle B_z\rangle/\partial t$ must also vanish, because on the right hand side of Eq. (4) only x and y derivatives occur, for which the average vanishes. We have therefore

$$\langle B_z\rangle = \mathrm{const} = B_0, \quad (14)$$

i.e. $\langle B_z\rangle$ is independent of z and t. Note that the periodic boundary conditions for $\boldsymbol{B}$ conserve the vertical magnetic flux, i.e. $\int dx\,dy\,B_z = \mathrm{const}$.

2.5. *Dimensionless quantities*

It is convenient to discuss properties of different models in terms of non-dimensional numbers. The most important one is the Rayleigh number,

$$\mathrm{Ra} = \frac{gd^4}{\kappa\nu}\frac{ds^{(0)}}{dz}, \quad (15)$$

where $\kappa = \mathscr{K}/\gamma\rho$ is the coefficient of thermal (or radiative) conductivity, $\nu = \mu/\rho$ the kinematic viscosity, and $s^{(0)}$ the entropy of the initial stratification. The entropy is measured in units of c_p with $s = \ln(p^{1/\gamma}/\rho)$. The entropy gradient for the initial stratification is given by $ds^{(0)}/dz = [1-(m+1)(1-1/\gamma)]d/z$. Note that $(\mathrm{Ra}/\mathrm{Pr})^{1/2}$ is the ratio of the diffusive time scale, $\tau_d = d^2/\nu$, to the convective time scale, $\tau_c = |N_{\mathrm{BV}}|^{-1}$, where $N^2_{\mathrm{BV}} = -gds/dz$ is the square of the local (generalized) Brunt-Väisälä frequency. $\mathrm{Pr} = \nu/\kappa$ is the Prandtl number and in all cases considered in this paper we keep $\mathrm{Pr} = 1$. From now on Ra denotes the Rayleigh number evaluated in the *middle* of the layer. In practice we prescribe Ra and determine κ and ν for a given stratification using Eq (15).

The strength of the initial vertical magnetic field is measured by the Chandrasekhar number,

$$Q = \frac{B_0^2}{\mu_0}\frac{d^2}{\mu\eta} \equiv (v_{A0}d/\nu_0)^2\,\mathrm{Pm}, \quad (16)$$

and the rotation rate is measured by the Taylor number,

$$\mathrm{Ta} = (2\Omega d^2/\nu_0)^2. \quad (17)$$

(Note that μ_0 is the induction constant and μ the viscosity.) v_{A0} is the initial Alfvén velocity at $z = z_0$ with $v_A = \langle \boldsymbol{B}^2/\mu_0\rho\rangle^{1/2}$. $\mathrm{Pm} = \nu_0/\eta$ is the magnetic Prandtl number, where $\eta = 1/\mu_0\sigma$ and $\nu_0 = \mu/\rho_0$ denotes the kinematic viscosity at the top layer for the initial stratification. (The magnetic Prandtl number used by Hurlburt and Toomre (1988) is $\zeta = \eta/\kappa = \mathrm{Pr}/\mathrm{Pm}$.) The relative strength of the Lorentz force and the Coriolis force is given by the Elsasser number, $\mathrm{El}=Q/\mathrm{Ta}^{1/2}$.

In addition to the control parameters Ra, Q, and Ta, the system is determined by the two Prandtl numbers, Pr and Pm, the stratification parameter χ, and by the ratio A of the width to the height of the box (aspect ratio).

The strength of the resulting convection is measured by the Nusselt number,

$$\mathrm{Nu} = (F_{\mathrm{tot}} - F_{\mathrm{ad}})/(F^{(0)}_{\mathrm{rad}} - F_{\mathrm{ad}}), \quad (18)$$

where $F_{\mathrm{tot}} = F_{\mathrm{conv}} + F_{\mathrm{rad}} + F_{\mathrm{kin}} + F_{\mathrm{visc}}$. The various fluxes are defined as positive quantities when flux is directed upwards. $F_{\mathrm{conv}} = -\gamma\langle\rho e u_3\rangle$ is the convective flux, $F_{\mathrm{kin}} = -\frac{1}{2}\langle\rho \boldsymbol{u}^2 u_3\rangle$ the kinetic flux, $F_{\mathrm{visc}} = \langle u_j\tau_{j3}\rangle$ the viscous flux, and $F_{\mathrm{rad}} = \mathscr{K}\partial\langle e\rangle/\partial z$ the radiative flux. $F^{(0)}_{\mathrm{rad}} = \mathscr{K}\Delta\langle e\rangle/\Delta z$ is the radiative flux, for a linear variation of e with depth, and $F_{\mathrm{ad}} = \mathscr{K}(\partial\langle e\rangle/\partial z)_{\mathrm{ad}}$ is the radiative flux for an adiabatic stratification.

The mean convective or turbulent velocity $u_t \equiv \langle\langle u^2\rangle\rangle^{1/2}$ is measured by the Mach number, $\mathrm{Ma} = u_t/c$, where the double angular brackets denote a combined horizontal and vertical average. The importance of advection relative to diffusion is measured by the Reynolds number $\mathrm{Re} = u_t d/\nu_0$, whilst the importance of advection relative to rotation is measured by the Rossby number, $\mathrm{Ro} = \mathrm{Re}/\mathrm{Ta}^{1/2}$.

3. Results of calculations in 2-D

In this section we discuss statistical properties of flows for different values of Ra, Ta, and χ, obtained in the two dimensional approximation. We compare some of these results with models of Hurlburt et al. For all cases in this section where a magnetic field is included we assume $Q = 72$ and $\mathrm{Pm} = 4$, i.e. $\zeta = 0.25$, which was also considered by Hurlburt & Toomre.

3.1. *Test-computations in 2-D with $\Omega = B = 0$*

We first performed calculations for an isothermal atmosphere neglecting rotation and magnetic fields. After introducing a local disturbance in entropy we observed evolving Brunt-Väisälä oscillations and gravity waves. We found good quantitative agreement with predictions from the linear theory of local perturbations in an isothermal atmosphere (Brandenburg, 1988).

Next we studied an unstable stratified polytropic layer, with a density contrast $\chi = 1.5$, taking Rayleigh numbers between 10^3 and 10^5. In all cases a stationary final state developed. Table 1 summarizes our results for the Nusselt, Reynolds, Mach numbers and other properties. The Reynolds number usually has its maximum close to the bottom of the model, because $\mathrm{Re} \propto \rho$. At the top layer the Mach number is maximal, because $\mathrm{Ma} \propto c^{-1}$ and c decreases upwards. The entropy gradient has its minimum somewhere in the middle layers, or slightly below.

The last run in Table 1 may be compared with results by Hurlburt et al. (1984, their Table 1, first line). The resulting Nusselt numbers and Mach numbers agree within 8% and the convective and kinetic flux within 5% accuracy. We note, however, that the number of convection cells does not always agree with the number given by Hurlburt et al. (1984). The number of rolls is obviously determined not only by the aspect ratio, but also by the initial conditions. We confirmed that starting with a single pair of convection rolls may also lead to a stable configuration. An example showing the evolution towards a final state with two pairs of cells is shown in Fig. 1, where we have taken as an initial condition a small local perturbation in entropy.

3.2. *Test-computations including magnetic fields*

We tested the magnetic part of the code by computing simple stationary and time-dependent MHD flows. Some of these test

Table 1. Summary of various quantities for a series of runs with different Rayleigh numbers ($\chi = 1.5$, $A = 3$). The maximum values of F_{conv}, F_{kin}, and F_{visc} and the minimum value of F_{rad} are given. Δs denotes the entropy difference between bottom and top of the final state. In the last column are the results obtained by Hurlburt et al. (1984) for Ra = 1.2 10^5 are given for comparison

Ra	10^3	2×10^3	5×10^3	10^4	5×10^4	10^5	HTM 84
Nu	1.6	2.4	3.3	3.9	7.0	8.0	7.4
Re	5.9	9.1	15	22	51	73	
Ma(max)	0.05	0.05	0.06	0.06	0.06	0.06	0.07
$\Delta\langle s\rangle$	0.063	0.037	0.028	0.023	0.017	0.014	
F_{rad}/F_{tot}	0.84	0.79	0.78	0.78	0.73	0.75	0.76
F_{conv}/F_{tot}	0.16	0.21	0.22	0.22	0.27	0.25	0.24
F_{kin}/F_{tot}	0.000	−0.001	−0.004	−0.004	−0.020	−0.016	−0.016
F_{visc}/F_{tot}	0.002	0.003	0.003	0.004	0.003	0.003	

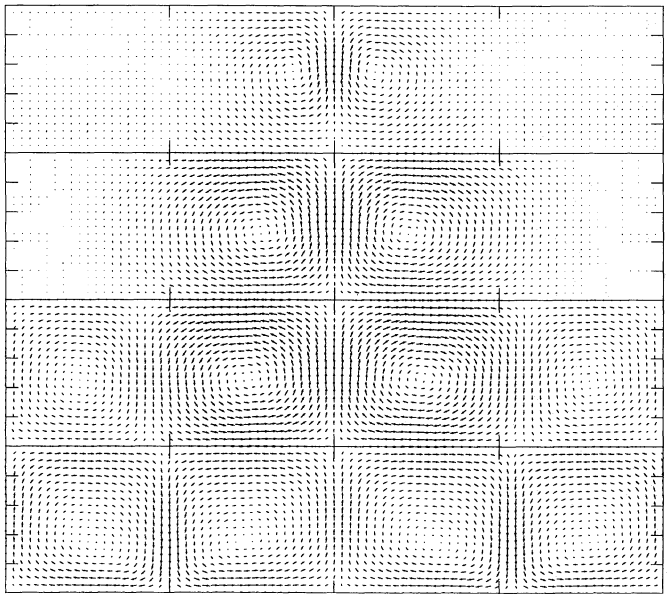

Fig. 1. Snapshots showing the evolution after introducing a small disturbance in entropy at the center of the computational domain with $A = 4$ in 2-D. (Ra = 10^5, $\chi = 1.5$ and $Q = 0$.) Time increases downwards. The last frame shows two pairs of convection cells after about 160 sound travel times

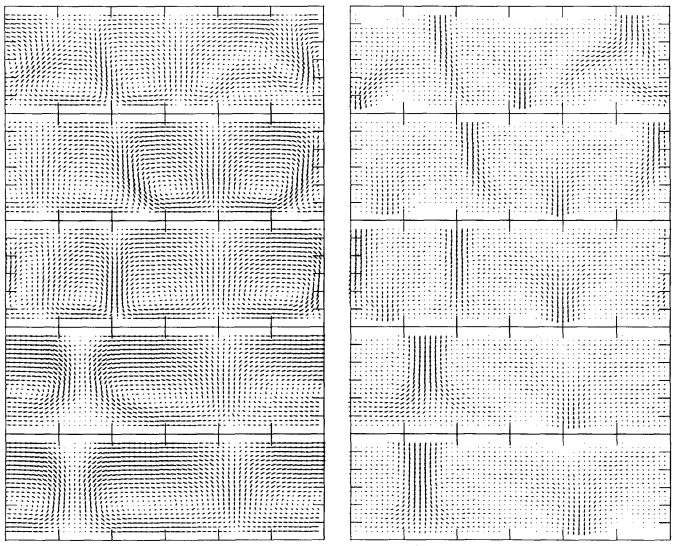

Fig. 2. Vector plots of the velocity (left) and magnetic field (right) showing the evolution of a weak and initially homogeneous vertical magnetic field affected by convection. (Ra = 10^5, $\chi = 11$, $A = 3$, $Q = 72$, and $P_m = 4$.) The time instants are 23, 44, 54, 93, 177 (time increases downwards). During an intermediate stage there are two flux tubes present which merge finally into a single one

calculations involved slightly modified boundary conditions for $\boldsymbol{u}$ and $\boldsymbol{B}$. We have computed horizontally propagating Alfvén waves and find good agreement between the propagation velocity of the wave pattern and the theoretical Alfvén velocity. Another test concerns the free decay of a vertical magnetic flux tube with a Gaussian distribution, for which we found the correct decay rate. (Because of the periodic boundary conditions the final state is a homogeneous field.) Finally we have computed a Hartmann flow with rigid upper and lower boundaries. This is essentially a 1-D problem only. The profile for the velocity and the magnetic field is in good agreement with the analytical solution (e.g. Jackson, 1962).

We then consider convective rolls with an initially vertical magnetic field. We choose the parameters Ra = 10^5 and $\chi = 11$, which allow a direct comparison with the results of Hurlburt and Toomre (1988, their Fig. 1, 2). In Fig. 2 we show the evolution of an initially homogeneous magnetic field affected by convection. During an intermediate stage there are two flux tubes present which finally converge into a single tube. The final result is in good agreement with that of Hurlburt and Toomre for the same case. Also the variation of magnetic pressure, $p_m = \boldsymbol{B}^2/2\mu_0$, the dynamic pressure, $p_d = \rho\boldsymbol{u}^2$, and the gas pressure, p, across the flux tube, depicted in Fig. 3 for $z = 0.15$ close to the surface, agrees with that of Hurlburt and Toomre (see their Fig. 2a). Other parameters of this model are summarized in the first column of Table 2.

3.3. Results in 2-D with rotation

We are interested in the effects of rotation, because, for example, the α-effect is only present with rotation. On the other hand, the

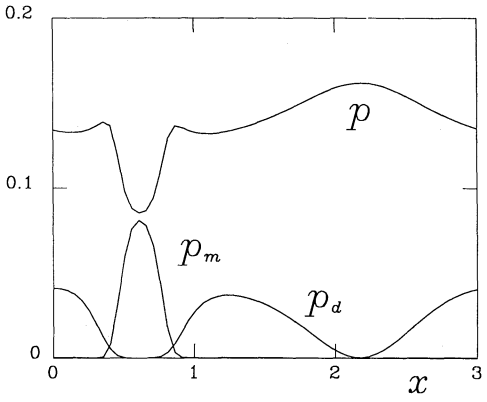

Fig. 3. The magnetic, dynamic, and gas pressure (p_m, p_d, and p, respectively) across the flux tube at $z = 0.15$ for the final stationary solution corresponding to the last panel in Fig. 2. (Ra = 10^5, $\chi = 11$, $A = 3$, $Q = 72$, and $P_m = 4$.) This picture is in agreement with Fig. 2 of Hurlburt and Toomre

Table 2. Summary of the various mean quantities for different runs where magnetic field is included ($Q = 72$). In the first three columns are listed 2-D runs with Pm = 4, whilst the last one contains the results of a 3-D run with Pm = 1

Ra	10^5	10^4	$2\,10^4$	10^5
Ta	0	10^4	10^4	10^4
χ	11	11	2	2
A	3	3	2	2
Nu	2.2	1.3	1.9	4.4
Re	5.5	6.0	10	40
Ma(max)	0.09	0.09	0.03	0.04
$\Delta\langle s\rangle$	0.431	0.500	0.075	0.040
F_{rad}/F_{tot}	0.79	0.90	0.85	0.77
F_{conv}/F_{tot}	0.27	0.11	0.15	0.23
F_{kin}/F_{tot}	−0.06	−0.006	−0.000	−0.003
$\langle u_x^2\rangle/u_t^2$	0.70	0.25	0.17	0.3
$\langle u_y^2\rangle/u_t^2$	0	0.49	0.34	0.3
$\langle u_z^2\rangle/u_t^2$	0.30	0.25	0.49	0.6
$\langle u_x u_y\rangle/u_t^2$	0	−0.30	−0.22	0.04
$\langle u_z^3\rangle/\langle u_z^2\rangle^{3/2}$	1.25	0.22	−0.04	0.1
$\langle u_z^4\rangle/\langle u_z^2\rangle^2$	5.0	3.2	2.3	2.5
$\langle B_x^2\rangle/B_0^2$	1.34	0.38	0.24	1.5
$\langle B_y^2\rangle/B_0^2$	0	0.02	0.72	1.5
$\langle B_z^2\rangle/B_0^2$	2.81	1.70	4.2	4
$\langle B_x B_y\rangle/B_0^2$	0	−0.02	−0.39	0.03
$\langle B_z^3\rangle/\langle B_z^2\rangle^{3/2}$	2.3	1.4	1.9	3
$\langle B_z^4\rangle/\langle B_z^2\rangle^2$	6.6	2.4	4.2	10

α-effect is fundamentally a 3-D phenomenon. Therefore we have not investigated the 2-D case with rotation very deeply.

Some results are summarized in the second and third column of Table 2. In the presence of rotation the Nusselt number is reduced and the critical Rayleigh number is increased (see Chandrasekhar, 1961). For example, for Ra = 10^4 and Ta = 10^5 the stratification is still stable. Therefore we have adopted in the following Ta = 10^4. The mean Reynolds numbers were still quite small (Re ≈ 6) and the Rossby number was only 0.1, i.e. the flow was strongly dominated by rotation. A strong correlation between u_x and u_y appears, because the velocity field is systematically stretched by the effect of rotation. However, this is an artifact of the 2-D nature of the flow allowing a non-vanishing y-component of the flow (and magnetic field), but making variations along the y-direction impossible. A strong $\langle u_x u_y\rangle$ correlation is not present in a true three dimensional flow (see the last column of Table 2 for a 3-D run considered in the following section).

4. Results for 3-D magneto-convection

In this section we present results obtained for three dimensional magneto-convection. The Rayleigh number was taken sufficiently large to lead to fully developed turbulent convective flows. We took an aspect ratio $A = 2$ and a density contrast $\chi = 2$. According to our experience, the resolution in the z-direction should be higher than in the horizontal directions. We chose a z resolution four times finer than the horizontal resolution, although a factor of two might have been adequate. It turns out that the upper limit we were able to treat with a resolution of $31 \times 31 \times 63$ mesh points was Ra = 10^5, which is about 300 times supercritical. We have kept the same Chandrasekhar number and Taylor number as in the 2-D runs, namely $Q = 72$ and Ta = 10^4. This corresponds to an Elsasser number El=0.72 which takes us into an astrophysically interesting regime (cf. Roberts, 1988). However, for the previous value $P_m = 4$ we found a critical accumulation of *magnetic* energy in the smallest scales. We therefore carried out most of the simulations with $P_m = 1$, but some were performed with $P_m = 2$ which is really at the border of what is attainable with the present resolution.

4.1. Properties of the flow

We describe here the results of a particular run with parameters as stated above. After about 30-50 sound travel times a statistically nearly stationary state developed. An example of the resulting flow and magnetic field vectors, projected onto a horizontal and vertical plane in the middle of the regime (upper and lower two panels, respectively), is shown in Fig. 4. The mean vertical density contrast is slightly stronger than in the initial polytropic state and the entropy becomes nearly constant except in a boundary layer of about 10% thickness of the total depth at the upper boundary (Fig. 5).

It is hard to visualize the behavior of an irregular time-dependent three dimensional flow. The irregularity of the flow may be demonstrated in terms of sections of the trajectories in phase space and its intersections with certain hyperplanes (Poincaré maps). An example is shown in Fig. 6 where we have plotted the x- and y-components of the velocity (a) and the magnetic field (b) measured in the middle of the computational box. The intersections with the planes $u_z = 0$ and $B_z = 0$ are marked in the right panel. The trajectories do not seem to approach any simple kind of attractor, but the simulation was not run for a very long time.

A more direct presentation of the rich temporal variations of the convection patterns is given by a sequence of snapshots of the u_z and B_z fields in a horizontal plane, which is shown in Fig. 7 for $z = 1.5$ (the middle of the box). The first snapshot is at $t = 80$ and the time between two pictures is about 15 sound travel times. The last twelve frames are for a magnetic viscosity half as large ($P_m = 2$) as in the first part of the run ($P_m = 1$).

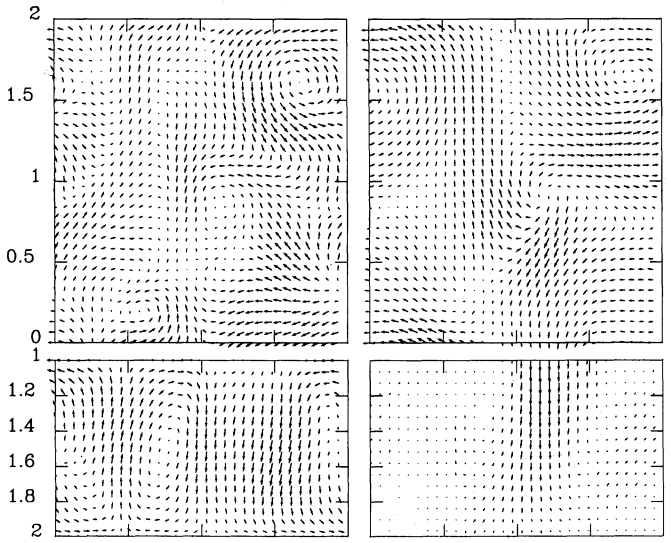

Fig. 4. Snapshot showing a 3-D flow at $t = 169$. In the upper two panels the velocity (left) and magnetic field vectors (right) are projected onto an $x-y$ plane at $z = 1.5$, and in the lower two panels similarly for an $x-z$ plane at $y = 1$

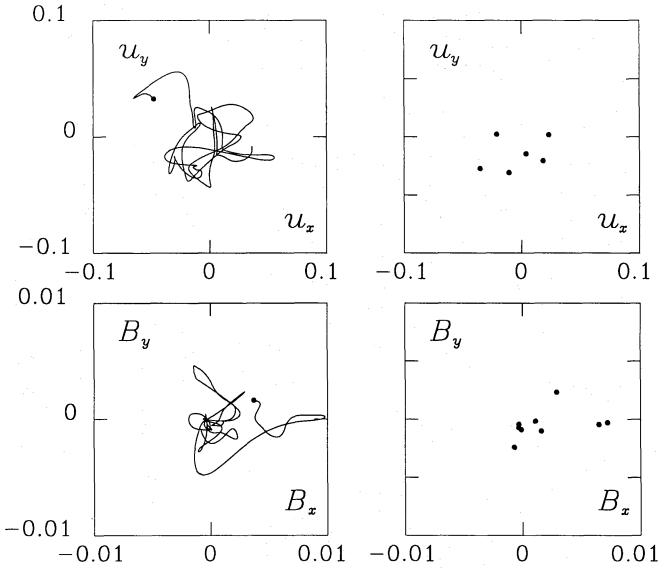

Fig. 6. A plot of the x- and y-components of the velocity (upper panel on the left) and the magnetic field (lower panel on the left) measured in the middle of the computational box. The starting point is marked by a dot ($t = 50$). Poincaré maps showing intersections with the planes $u_z = 0$ and $B_z = 0$ are given respectively in the right panels

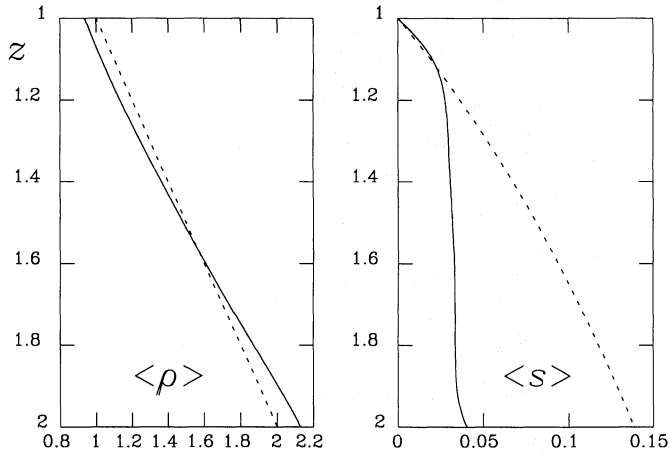

Fig. 5. The mean stratification of density and entropy for fully developed convection (solid lines) in comparison with the initial state (dotted lines). The entropy is normalized to zero at the top

4.2. The Reynolds and Maxwell stress tensor

Other important properties may be obtained by considering certain correlation functions. The simplest of these are the components of the Reynolds and Maxwell stress tensor, $\langle u_i' u_j' \rangle$ and $\langle B_i' B_j' \rangle$, respectively, where $\boldsymbol{u}$ and $\boldsymbol{B}$ are split into mean and fluctuating parts,

$$\boldsymbol{u} = \langle \boldsymbol{u} \rangle + \boldsymbol{u}' \quad \text{and} \quad \boldsymbol{B} = \langle \boldsymbol{B} \rangle + \boldsymbol{B}'. \tag{19}$$

The quantities $\langle u_i' u_j' \rangle$ and $\langle B_i' B_j' \rangle$ are still functions of t and z. We display them in three different ways.

Fig. 8 shows contour maps of these functions in the $t-z$-plane. There are temporal variations visible in all six quantities, the time scale of which is comparable to the rotation period, $2\pi/\Omega = 92$ sound travel times) and to the Alfvén time, d/v_A (≈ 50 sound travel times). (The turnover time, d/u_t, ≈ 20 sound travel times.)

The z-average of these quantities, is plotted against time in Fig. 9. We note that the values $\langle u_i'^2 \rangle$ and $\langle B_i'^2 \rangle$ seem to decay slowly. These slow variations may either be physical and reflect some thermal adjustment associated with the diffusion time scale, or they may be due to the fact that energy is not exactly conserved numerically.

The non-diagonal components vary about zero, and only the horizontal stress $\langle u_x' u_y' \rangle$ has slightly more contributions from positive values. The same seems to be the case also for $\langle B_x' B_y' \rangle$, but the evidence is less strong here. On the average these cross correlations are therefore quite small, which is in contrast to the 2-D results with rotation. The results for both cases may be compared in the third and fourth column of Table 2.

The upper two panels of Fig. 10 shows the variation of the rms-values of $\boldsymbol{u}$ and $\boldsymbol{B}$ with depth. We have taken the time average over the interval $t = 50...270$. The data for later times are excluded here, because they were obtained with different value of $\mathrm{P_m}$. $\boldsymbol{B}$ is measured by the Alfvén speed v_A. The variation with depth is relatively small. Note that the rms magnetic field in the fully developed turbulent states exceeds the initial field (dotted line) by almost a factor of three.

4.3. Anisotropy

In the theory of stellar differential rotation the degree of anisotropy of the motions is important.

The anisotropy of turbulent motions may be measured by the quantity (in spherical coordinates)

$$A_V \approx 2\tau (\langle u_\phi'^2 \rangle - \langle u_r'^2 \rangle) \tag{20}$$

(cf. Rüdiger, 1980, Eq.(4.11)). For a stress-free rotation law we have $\partial \ln \Omega / \partial \ln r = A_V / v_t$, where $v_t = \frac{1}{3}\tau u_t^2$ and τ denotes a

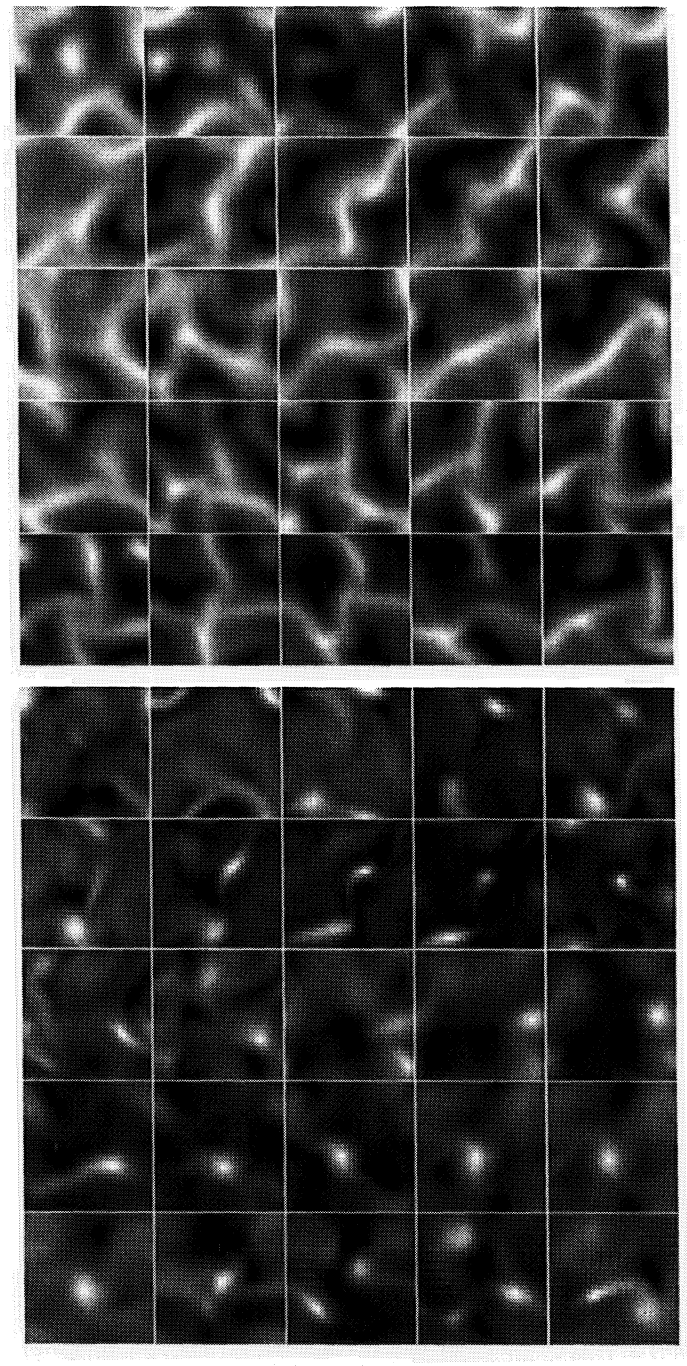

Fig. 7. A series of snapshots of the u_z (upper part) and B_z (lower part) fields in a horizontal plane for $z = 1.5$. Bright tones correspond to a positive sign of u_z and B_z (i.e. to a downward oriented field). The first snapshot is at $t = 80$ and the time between two pictures is about 15. The time instants are 80, 95, 109, 124, 139, 150, 159, 174, 188, 203, 234, 249, 265, 283, 298, 314, 324, 333, 348, 364, 379, 394, 408, 424, and 439. The magnetic diffusivity for the flow depicted in the last twelve frames is two times smaller than during the first part of the run

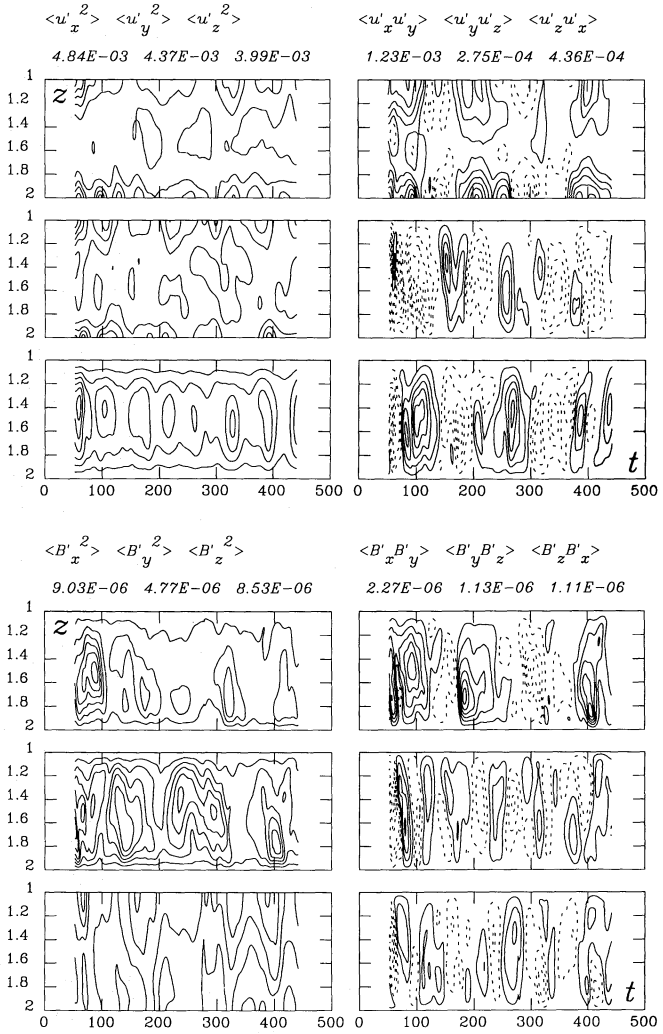

Fig. 8. Plots of the functions $\langle u_i' u_j' \rangle$ (upper part) and $\langle B_i' B_j' \rangle$ (lower part) as contour maps in the $t - z$-plane. Dotted lines refer to negative values. The numbers given in the title denote the maxima values in each panel

correlation time. Since in our 3-D cases the x- and y-directions are equally preferred, we consider instead of Eq. (20) the expression

$$\Lambda_V / 3v_t \approx (\langle u_x'^2 \rangle + \langle u_y'^2 \rangle - 2\langle u_z'^2 \rangle)/u_t^2. \quad (21)$$

In the second row of Fig. 10 we have plotted $\Lambda_V / 3v_t$ from Eq. 21 and, in analogy to that, also the quantity $(\langle B_x'^2 \rangle + \langle B_y'^2 \rangle - 2\langle B_z'^2 \rangle)/B_0^2$, abbreviated in the Figure to M_V. The extrema of both functions occur at the upper and lower boundaries and their shape resembles that of a cosine. If in a stellar convection zone the profile of $\Lambda_V / 3v_t$, and thus of the gradient of angular velocity, were really like a cosine, then the profile of the angular velocity would be roughly sinusoidal. This is indeed the profile emerging from recent results of helioseismology (see Dziembowski et al., 1989, their Fig. 2). With such a profile is has also been possible to construct solar kinematic dynamo models (Brandenburg & Tuominen, 1988).

4.4. Skewness and flatness

Two important quantities describing a turbulent flow are the skewness and flatness, $\langle u_i'^3 \rangle / \langle u_i'^2 \rangle^{3/2}$ and $\langle u_i'^4 \rangle / \langle u_i'^2 \rangle^2$, respectively. These quantities describe the deviation of the flow from isotropy and Gaussian statistics. It turns out that the skewness of the vertical component of the velocity has a positive maximum

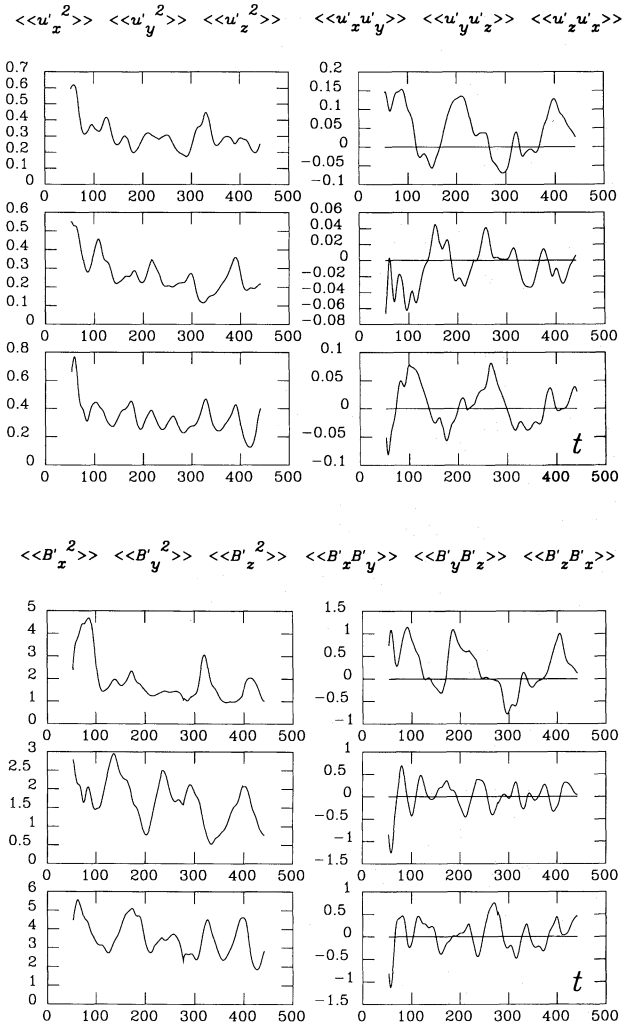

Fig. 9. The time dependence of the functions $\langle\langle u_i' u_j' \rangle\rangle$ (normalized to u_t^2) (upper part) and $\langle\langle B_i' B_j' \rangle\rangle$ (normalized to B_0^2) (lower part)

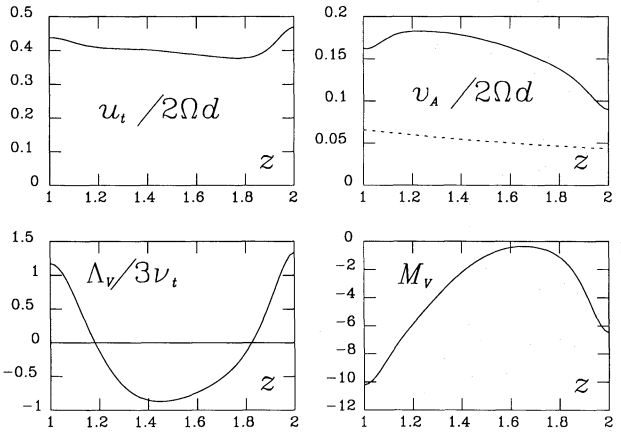

Fig. 10. *Upper panels:* Variation of u_t and v_A with depth. Both functions are normalized with $2\Omega d$. *Lower panels:* Plots of Λ_V (normalized to $3\nu_t$) and of the quantity $(\langle B_x'^2 \rangle + \langle B_y'^2 \rangle - 2\langle B_z'^2 \rangle)/B_0^2$ (abbreviated in the figure with M_V)

near the bottom of the domain. This result is qualitatively in agreement with that of Eidson et al. (1986) for incompressible Rayleigh-Bénard convection with $\mathrm{Ra} = 10^5$. The reason why the skewness is positive near the lower boundary is that the density stratification induces the formation of concentrated downdrafts, immersed in a background of gentler ascending fluid (cf. Stein & Nordlund, 1989).

It is also possible to define magnetic skewness and magnetic flatness, $\langle B_i'^3 \rangle / \langle B_i'^2 \rangle^{3/2}$ and $\langle B_i'^4 \rangle / \langle B_i'^2 \rangle^2$, respectively. There is a strong positive skewness of the vertical component of the magnetic field in the upper part, which is obviously due to the field concentration.

The flatness of the three velocity components is about 2, which is also in agreement with values quoted by Eidson et al. The magnetic flatness is much higher, between 5 and 20. The flatness is a measure of the intermittency of the velocity or the magnetic field. We thus conclude that the magnetic field is about three times more intermittent than the velocity field (for $\mathrm{P_m} = 1$). For smaller magnetic diffusivity ($\mathrm{P_m} = 2$) the degree of magnetic intermittency turns out to be even larger. Some results for the skewness and flatness are included in Table 2.

4.5. *Helicity*

We next investigate the various helicities of the flow and their distribution with height. Helicity is widely believed to be an important ingredient for dynamo action. According to the theory of Steenbeck et al. (1966) the kinetic helicity $\langle \boldsymbol{\omega}' \cdot \boldsymbol{u}' \rangle$ should be negatively proportional to α, where $\boldsymbol{\omega}' = \mathrm{curl}\, \boldsymbol{u}'$ and α parameterizes the functional dependence of the mean electromotive force $\mathscr{E} \equiv \langle \boldsymbol{u}' \times \boldsymbol{B}' \rangle$ on the mean magnetic field $\langle \boldsymbol{B} \rangle$, in the simplest form via

$$\mathscr{E} = \alpha \langle \boldsymbol{B} \rangle. \tag{22}$$

Furthermore, when the magnetic field becomes strong one expects a back-reaction on the α-effect governed by magnetic helicity $\langle \boldsymbol{J}' \cdot \boldsymbol{B}' \rangle$ which gives

$$\alpha = -\frac{1}{3}\tau (\langle \boldsymbol{\omega}' \cdot \boldsymbol{u}' \rangle - \langle \boldsymbol{J}' \cdot \boldsymbol{B}' \rangle / \langle \rho \rangle) \tag{23}$$

(Pouquet & Patterson, 1978), where $\langle \boldsymbol{J}' \cdot \boldsymbol{B}' \rangle$ acts against $\langle \boldsymbol{\omega}' \cdot \boldsymbol{u}' \rangle$ if both have the same sign.

From our simulations we have evaluated the two helicities mentioned above and also the cross helicity $\langle \boldsymbol{u}' \cdot \boldsymbol{B}' \rangle$, which is a measure of the degree of linkage of the vortex lines of the $\boldsymbol{u}$-field with the lines of force of the $\boldsymbol{B}$-field (Moffatt, 1978). Fig. 11 displays the dependence of the various helicities on z and t as contour maps. We find a systematic separation of positive and negative kinetic helicity in the upper and lower layers of the model, which is obviously due to the influence of rotation. We have confirmed this by rerunning the same case with opposite direction of rotation, which leads to a reversed sign of the helicities. The magnetic helicity has a similar variation with depth, but we discovered to our surprise that the sign is opposite to that of the kinetic helicity. The nature of this feature will be discussed in more detail in Sect. 4.7.

4.6. *The balance of forces*

We have looked at the z-components of the kinetic and magnetic interaction terms $\langle \boldsymbol{\omega}' \times \boldsymbol{u}' \rangle_z$ and $\langle \boldsymbol{J}' \times \boldsymbol{B}' \rangle_z$. It turns out that these also have opposite sign (cf. the right hand panel of Fig.

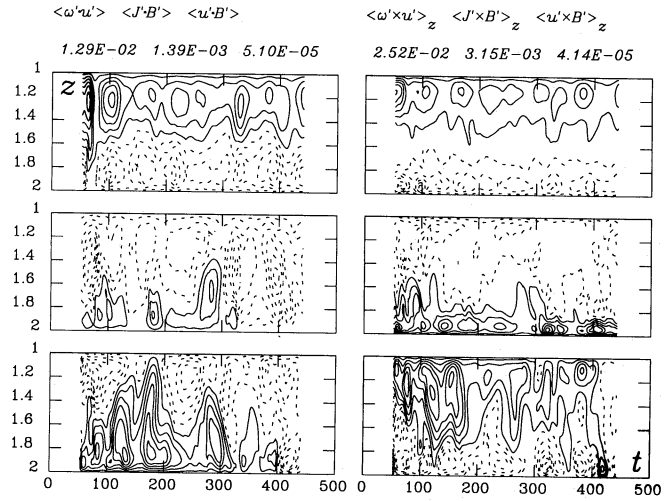

Fig. 11. The spatial and temporal dependence of kinetic, magnetic and cross helicity (left panels) and the z-components of the kinetic and magnetic interaction terms together with the z-component of the mean electromotive force. Note the systematic separation of positive and negative values on all four contour maps

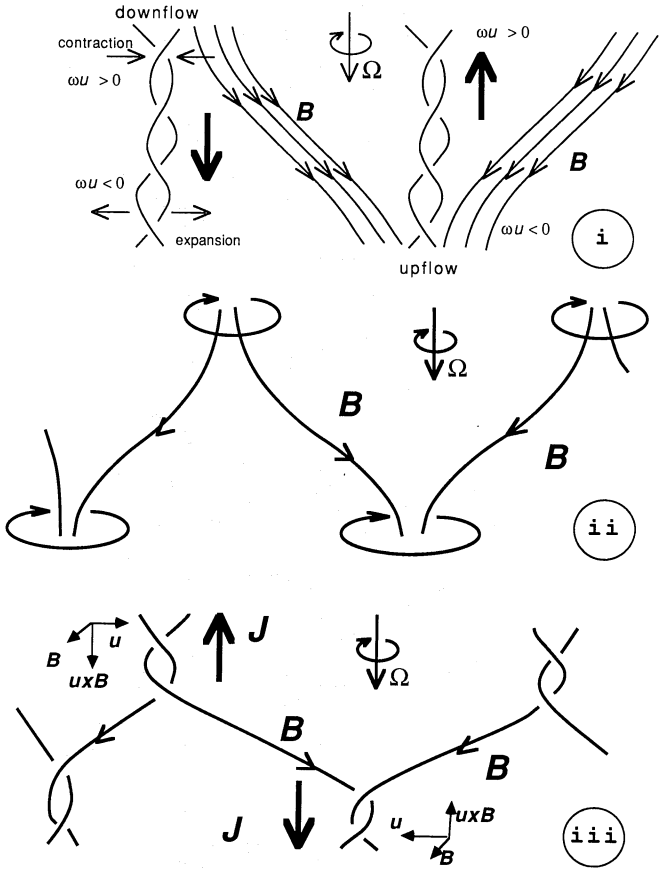

Fig. 12. A sketch of the field topology showing the twisting of field lines under the influence of rotation. See text

11), i.e. there is no balance between magnetic and kinetic forces. An approximate balance between kinetic and magnetic forces appears in nearly stationary flows in the absence of buoyancy effects, for instance in incompressible mean-field dynamo models (cf. Brandenburg et al., 1989c).

We have checked the importance of each term in the horizontally averaged momentum equation and find that the magnetic and kinetic forces are balanced by the "buoyancy force" $(-\rho^{-1}\nabla p + \boldsymbol{g})$. Near the bottom the buoyancy force is directed upwards and in the top layers, because of buoyancy braking it is directed downwards. In our simulation the magnetic and kinetic force is directed opposite to the net buoyancy force. The residual force on the rhs of the horizontally averaged momentum equation, i.e. $\partial\langle u_z\rangle/\partial t$, is relatively small compared to the other terms.

4.7. *A cartoon picture of the field line twisting*

A sketch of the velocity and magnetic field configuration is given in Fig. 12. As a consequence of the Coriolis force, $\boldsymbol{\omega}$ and $\boldsymbol{\Omega}$ are parallel in regions of converging flow and antiparallel in regions of diverging flow. Thus, there is positive kinetic helicity $\langle\boldsymbol{\omega}'\cdot\boldsymbol{u}'\rangle$ in the upper parts and negative helicity in the lower parts of the layer. Moreover, since the magnetic field is concentrated mainly in the converging regions, the vorticity induced on $\boldsymbol{B}$ is always oriented into the same direction (downwards), and, at first glance, the only twisting of the magnetic field expected would be due to differences in vorticity between the top and bottom layers; cf. panel (i).

However, because field lines are anchored at different horizontal positions in the top and bottom layers, a much more efficient winding-up of field lines occurs; cf. panels (ii) and (iii). At the upper boundary the associated current is directed upwards, i.e. $\langle\boldsymbol{J}'\cdot\boldsymbol{B}'\rangle < 0$, and at the lower one downwards, i.e. $\langle\boldsymbol{J}'\cdot\boldsymbol{B}'\rangle > 0$. Thus, the signs of kinetic and magnetic helicity are opposite to each other.

Panel (iii) of Fig. 12 also depicts the orientation of the *horizontal* parts of the velocity and magnetic field vectors. In the upper layers, around the regions of converging flow, the horizontal parts of $\boldsymbol{u}$ and $\boldsymbol{B}$ lead to a downward oriented $\boldsymbol{u}\times\boldsymbol{B}$, whilst in the lower layers $\boldsymbol{u}\times\boldsymbol{B}$ is pointing upwards, in accordance with Fig. 11.

4.8. *The interplay between velocity and magnetic field*

Let us now analyze further the correlation between $\boldsymbol{u}$ and $\boldsymbol{B}$. B_z is concentrated in the converging regions, which near the upper surface coincide with the downdrafts. Thus, close to the upper boundary the vertical components of $\boldsymbol{u}$ and $\boldsymbol{B}$ point in the same direction. However, it turns out that the cross helicity $\langle\boldsymbol{u}'\cdot\boldsymbol{B}'\rangle$ is negative (see Fig. 11). Moreover, one would expect the net e.m.f. to vanish, which is not the case either. Therefore, obviously, the horizontal parts of both fields play an important role. In the following we discuss these horizontal field components in more detail.

Figures 13 and 14 show projections of the fields $\boldsymbol{u}$, $\boldsymbol{\omega}$, $\boldsymbol{B}$, and $\boldsymbol{J}$ onto horizontal planes at the levels $z = 1.14$ and $z = 1.9$, respectively. Let us first concentrate on the flow geometry in the upper layer (Fig. 13). We want to show qualitatively why there is a non-vanishing positive vertical e.m.f., $\mathcal{E}_z$. First, the field is mainly vertical in the downdrafts (see third row in Fig. 13) and therefore does not contribute much to $\mathcal{E}_z$. A significant horizontal magnetic field is present only in the updrafts and in the regions between up- and downdrafts. In the vector plots of Figs. 13 (first and third row) we have marked the line $u_z = 0$.

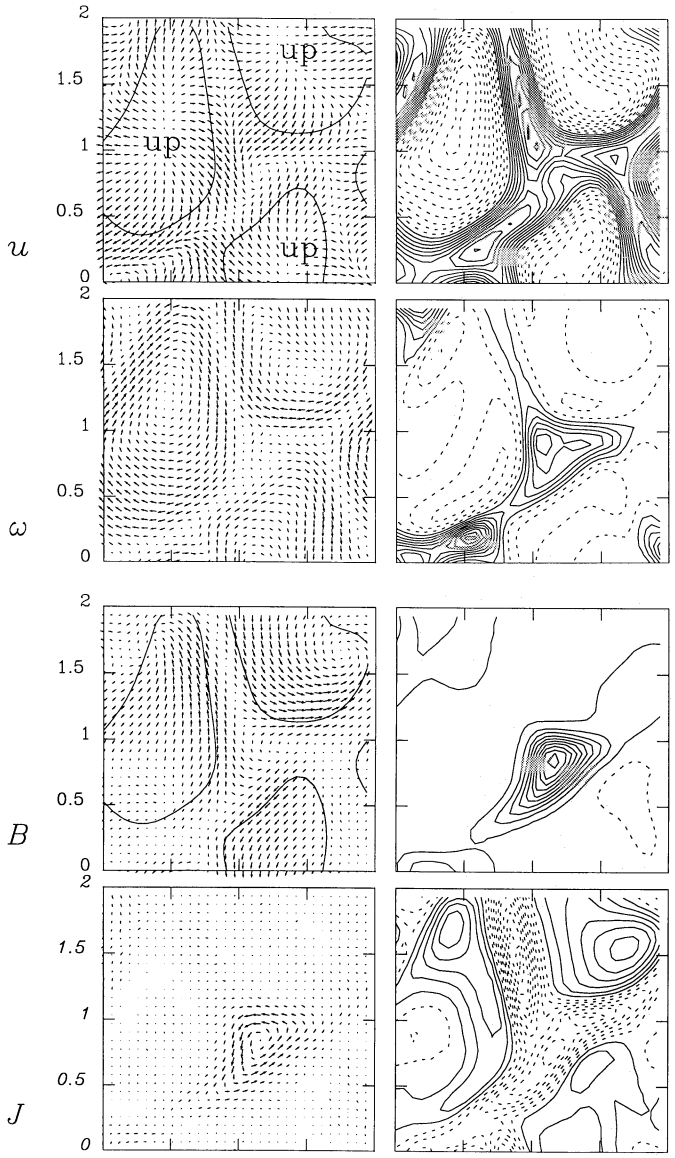

Fig. 13. Snapshot at $t = 169$ showing the fields $\boldsymbol{u}$, $\boldsymbol{\omega}$, $\boldsymbol{B}$ and $\boldsymbol{J}$, at the level $z = 1.14$. On the left hand side are projections of the field vectors in the $x - y$-plane (view from below). For the $\boldsymbol{u}$- and $\boldsymbol{B}$-fields a single contour plot $u_z = 0$ is superimposed marking the up- and downdrafts. On the right hand side contours of the z-component of the corresponding field are plotted

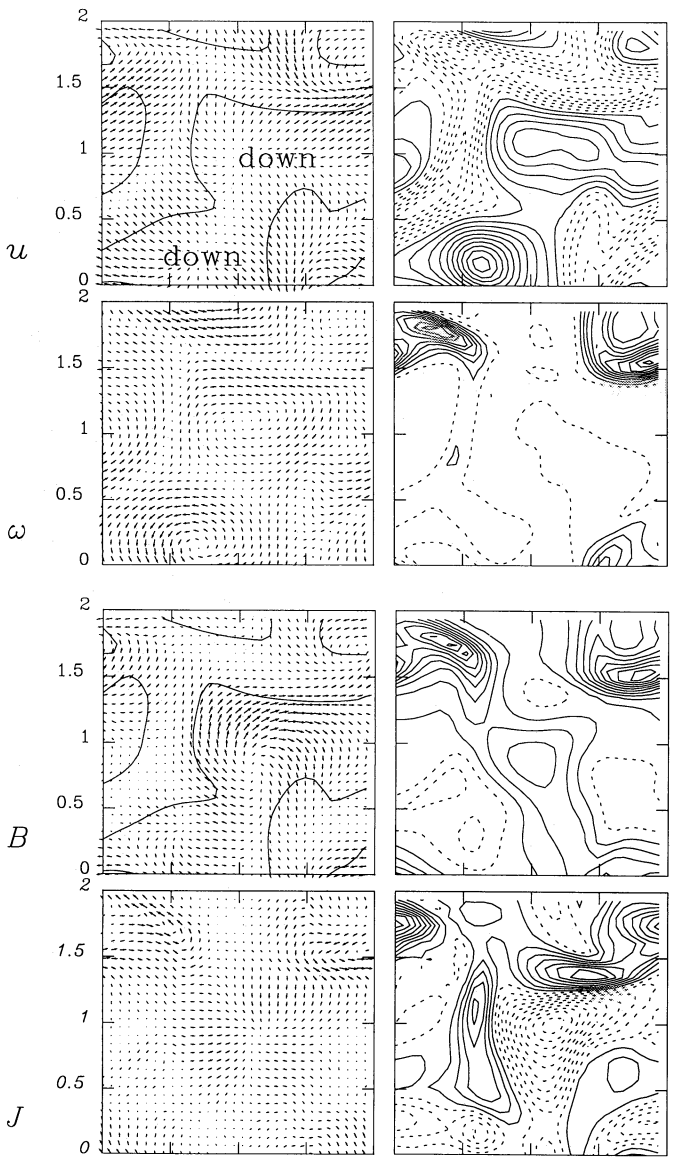

Fig. 14. Same as Fig. 13 but at the level $z = 1.9$. Note that now the updrafts are topologically connected

We see that the horizontal components of the magnetic field are almost parallel to the contours $u_z = 0$. The field vectors circle the contours $u_z = 0$ in a counterclockwise sense, when looking from below. Along and inside these contours the flow is diverging, leading so to $u_x B_y > 0$ and $u_y B_x < 0$. This means that $\mathscr{E}_z > 0$ in the top layers.

The situation at the bottom layer is different in some respects. Here the updrafts are topologically connected, whilst at the top the downdrafts are connected. The horizontal components of the magnetic field are again parallel to the contours $u_z = 0$, but the field vectors now circle the contours in a clockwise sense (looking from below). However, in both cases the flow is expanding outwards across the closed contours $u_z = 0$ (cf. in Figs. 13 and 14). Since the orientation is changed only for $\boldsymbol{B}$, and not for $\boldsymbol{u}$, we now have a reversed sign of $\mathscr{E}_z$ (i.e. $\mathscr{E}_z < 0$). The situation in Figs. 13 and 14 is in qualitative agreement with the simple cartoon picture (Fig. 12).

5. Mean-field transport coefficients and dynamo

To explain the large scale magnetic fields and flows in the Sun, the usual approach is to consider only mean values of the velocity and magnetic fields, and to solve directly the equations governing these mean fields. However, this involves ill-known quantities such as $\mathscr{E}$ and the Reynolds and Maxwell stress tensors. The hope is that these quantities may be expressed as functionals of the mean field itself. The full expressions for $\mathscr{E}$ can be quite complicated and Eq. (22) is only a very simple example of such a relationship. In this section we discuss the possibilities for evaluating α from the simulated data and apply the results to solve the mean-field induction equation.

5.1. The α-effect

Let us assume here the validity of (22). We may solve this equation for α to obtain

$$\alpha = \mathscr{E} \cdot \langle \boldsymbol{B} \rangle / \langle \boldsymbol{B} \rangle^2. \tag{24}$$

Adopting in Eq. (24) combined horizontal and temporal averages we find for α the profile shown in Fig. 15. We have displayed α in units of η/d which shows immediately that the value for the dynamo number $C_\alpha \equiv \max(\alpha d/\eta)$ is about ten (≈ 11.8).

We have compared this result with the profile of the kinetic helicity which is also averaged over time (lower panel in Fig. 15). Both functions look similar, they vanish at the boundaries and have a transition through zero somewhere in the lower half. Note, however, that α and $\langle \boldsymbol{\omega}' \cdot \boldsymbol{u}' \rangle$ have the same sign, which is in contrast to results of first order smoothing (Steenbeck et al., 1966, see also Eq. (23)). This is a consequence of the winding-up of field lines in our simulation, as discussed in the previous section. Such topological effects are not covered by first order smoothing, but occur once higher order correlations are included in the closure equations (Moffatt, 1974; Krause & Rädler, 1980).

Let us nevertheless compare the magnitude of α with first order smoothing results. The quantity $\alpha d/\eta$ is expected to scale with $\mathrm{P_m Ta}^{1/2}$ (cf. Brandenburg et al., 1989c). By comparing the two panels in Fig. 15 we find

$$\alpha d/\eta \approx 0.1 \mathrm{P_m Ta}^{1/2} \langle \boldsymbol{\omega}' \cdot \boldsymbol{u}' \rangle / 2\Omega u_t, \tag{25}$$

or $\alpha \approx 0.1\tau \langle \boldsymbol{\omega}' \cdot \boldsymbol{u}' \rangle$, where $\tau = d/u_t$ is assumed. Thus, α determined in this way is about five times smaller than the value obtained from the often adopted estimate $\max(\alpha) \approx \Omega d$, which is a crude simplification (e.g. correlation length is equal to d) of an more complicated expression derived by Krause (1967).

5.2. Comparison with mean-field models

Taking the horizontal average of Eq. (4) we obtain for the three components of $\langle \boldsymbol{B} \rangle$

$$\begin{aligned}
\partial_t \langle B_x \rangle &= \partial_z [\langle u_x \rangle \langle B_z \rangle - \langle u_z \rangle \langle B_x \rangle] - \partial_z \mathscr{E}_y + \eta \partial_z^2 \langle B_x \rangle, \\
\partial_t \langle B_y \rangle &= \partial_z [\langle u_y \rangle \langle B_z \rangle - \langle u_z \rangle \langle B_y \rangle] + \partial_z \mathscr{E}_x + \eta \partial_z^2 \langle B_y \rangle, \\
\partial_t \langle B_z \rangle &= 0.
\end{aligned} \tag{26}$$

These equations may be simplified formally by defining complex variables $\tilde{B} = \langle B_x \rangle + \mathrm{i}\langle B_y \rangle$, $\tilde{u} = \langle u_x \rangle + \mathrm{i}\langle u_y \rangle$, and $\tilde{\mathscr{E}} = \mathscr{E}_x + \mathrm{i}\mathscr{E}_y$, which leads to

$$\partial_t \tilde{B} = B_0 \partial_z \tilde{u} - \partial_z (\langle u_z \rangle \tilde{B}) + \mathrm{i} \partial_z \tilde{\mathscr{E}} + \eta \partial_z^2 \tilde{B}. \tag{27}$$

A similar equation has been studied by Krause and Meinel (1988) for the case $\tilde{u} = \langle u_z \rangle = B_0 = 0$ and $\tilde{\mathscr{E}} = \alpha \tilde{B}$ with $\alpha = \text{const}$ (α^2-dynamo), where the critical value of $\alpha d/\eta$ is $C_\alpha^{\mathrm{crit}} = 2\pi$. This is half the value for $\alpha d/\eta$ found from Eq (24). However, because of the presence of a non-vanishing $\langle B_z \rangle$, it is not correct to speak here about a self-excited dynamo.

In our case α is not constant and changes sign. The solutions are then typically oscillatory with somewhat higher critical dynamo numbers (for example, when α is a symmetric step function profile then $C_\alpha^{\mathrm{crit}} = 8.01$ with a period of 0.445 diffusion times, cf. Brandenburg et al., 1989a). If we use the α profile of Fig. 15 and then put $\tilde{u} = \langle u_z \rangle = B_0 = 0$, we find (numerically) the solution to be 15% supercritical with a period of 0.79 diffusion times, which corresponds to 385 sound travel times.

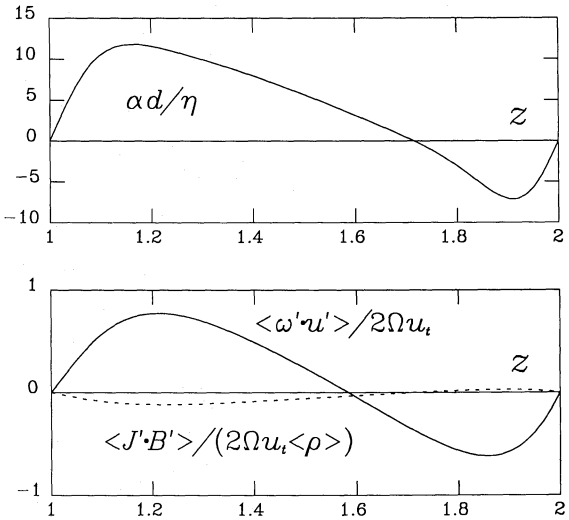

Fig. 15. The profile of α obtained from Eq. (24) (upper panel) compared with the profile of the kinetic helicity (lower panel). The shape and the location of the zero-transition is approximately similar in both cases

It is evident that the expression adopted here for α is much too simple to reproduce the results of the simulations for $\langle B_x \rangle$ and $\langle B_y \rangle$. This is demonstrated in Fig. 16, where we have plotted different solutions of Eq. (26) for $\langle B_x \rangle$ and $\langle B_y \rangle$ at $z = 1.48$ (upper and lower panel, respectively). The initial condition is taken from the simulation at $t = 100$. Solid lines give the result when the (time dependent) function $\mathscr{E} = \langle \boldsymbol{u}' \times \boldsymbol{B}' \rangle$ is evaluated from the simulation. We note that this solution reproduces accurately the functions $\langle B_x \rangle$ and $\langle B_y \rangle$ taken directly from the simulation. The influence of the mean velocity $\langle \boldsymbol{u} \rangle$ is only small. This is demonstrated by dashed lines representing the case where $\langle \boldsymbol{u} \rangle$ is neglected (but $\mathscr{E}$ included). In contrast, neglecting $\langle \boldsymbol{u}' \times \boldsymbol{B}' \rangle$ (dotted lines) leads to clear deviations from the solid curve on a short time scale. It seems, however, that on a longer time scale the dotted curves follow the solid ones. That is, short-term fluctuations are smoothed out. The dot-dash lines refer to the case where $\langle \boldsymbol{u}' \times \boldsymbol{B}' \rangle$ is replaced by $\alpha \langle \boldsymbol{B} \rangle$. In particular in the upper panel one sees a small part of a sinusoidal (overstable) oscillation. Clearly, the α-term over-represents $\mathscr{E}$, meaning that either α should be smaller or that it should be quenched by the magnetic field (nonlinear feedback).

In any case, the fact that the time scale of the α-effect dynamo is much longer than the convective time scale indicates that we should also formulate the mean-field equations for time averages, in such a way that a time dependence on a longer time scale is retained.

Finally we note that rerunning a simulation with negative Ω confirms our expectation that $\langle \boldsymbol{\omega}' \cdot \boldsymbol{u}' \rangle$ and α then both reverse sign compared to the case with positive Ω.

5.3. Anisotropy of α

We have assumed so far that α is isotropic. This is certainly not the case for Rayleigh-Bénard convection with impenetrable walls. Instead of using Eq. (22) it might be more appropriate to use, for example,

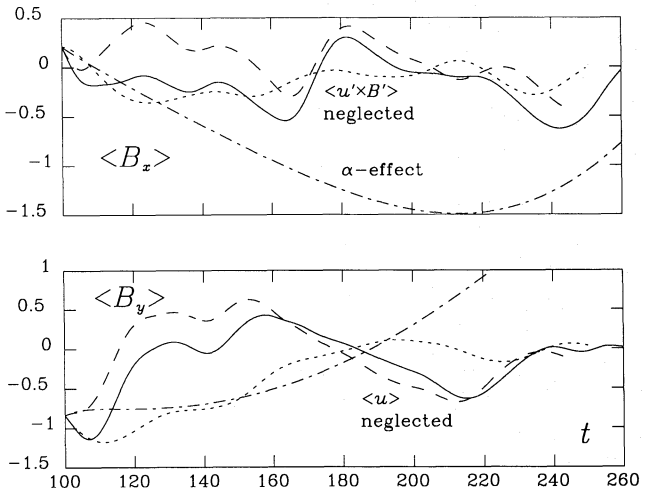

Fig. 16. Solutions of Eq. (26) for $\langle B_x \rangle$ and $\langle B_y \rangle$ (scaled by a factor of thousand) at $z = 1.48$. The different lines are explained in the text and also with key words in one of the two panels

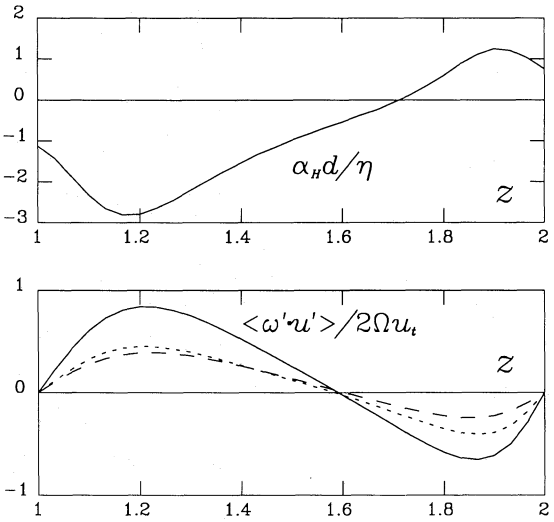

Fig. 17. The profile of α_H obtained as a solution of Eq. (28) (upper panel) compared with the profile of the kinetic helicity (lower panel). The dotted and dashed curves in the lower panel denote $\langle \boldsymbol{\omega}'_H \cdot \boldsymbol{u}'_H \rangle$ and $\langle \boldsymbol{\omega}'_V \cdot \boldsymbol{u}'_V \rangle$, respectively.

$$\mathcal{E} = \alpha_H \langle \boldsymbol{B}_H \rangle + \alpha_V \langle \boldsymbol{B}_V \rangle, \tag{28}$$

where $\langle \boldsymbol{B}_H \rangle = (\langle B_x \rangle, \langle B_y \rangle, 0)$ and $\langle \boldsymbol{B}_V \rangle = \hat{\boldsymbol{z}} B_0$. Note that *only* α_H enters into Eq. (26). In order to determine α_H we consider an initially horizontal magnetic field $(0, B_0, 0)$ replacing the upper and lower boundary conditions $B_y = 0$ by $B_y = B_0$. The result for α_H is shown in Fig. 17. We have plotted in the lower panel the kinetic helicity (solid line) as well as the horizontal and vertical parts of the helicity, $\langle \boldsymbol{\omega}'_H \cdot \boldsymbol{u}'_H \rangle$ and $\langle \boldsymbol{\omega}'_V \cdot \boldsymbol{u}'_V \rangle$ (dotted and dashed lines, respectively). It turns out that α_H is now a negative multiple of the helicity and it is about four times smaller in magnitude than α_V. This result for the sign of α_H is in agreement with predictions of mean-field theory.

The crucial question is whether this anisotropy of α is due to the preferred direction imposed by $\boldsymbol{g}$, $\boldsymbol{\Omega}$, or by both of them. In order to answer this question one has to investigate the α-effect for different Rossby numbers and for various angles between $\boldsymbol{\Omega}$ and $\boldsymbol{g}$. We have made a trial run for $\hat{\boldsymbol{\Omega}} \cdot \hat{\boldsymbol{g}} = \cos 75°$ and $\mathrm{Ra} = \mathrm{Ta} = 10^4$, which gives a 2.3 times larger inverse Rossby number ($\mathrm{Ro} = 0.17$) than in the previous case ($\mathrm{Ro} = 0.4$). The result is that in this case the anisotropies given by the preferred directions due to $\boldsymbol{g}$ and $\boldsymbol{\Omega}$ are both of similar magnitude and both contribute to the negative sign of the ratio α_H/α_V.

5.4. *The turbulent magnetic diffusivity*

In Eq. (22) we have neglected the *turbulent* magnetic diffusivity, η_t. Including this effect leads to

$$\mathcal{E} = \alpha \langle \boldsymbol{B} \rangle - \eta_t \mu_0 \langle \boldsymbol{J} \rangle \tag{29}$$

(Steenbeck et al., 1966), where anisotropic effects are again neglected. It turns out that a good approxiation is simply $\eta_t \mu_0 = -\mathcal{E} \cdot \langle \boldsymbol{J} \rangle / \langle \boldsymbol{J} \rangle^2$, because $(\langle \boldsymbol{J} \rangle \cdot \langle \boldsymbol{B} \rangle)^2 \ll \langle \boldsymbol{J} \rangle^2 \langle \boldsymbol{B} \rangle^2$. Adopting again combined horizontal and temporal averages, we find $\eta_t \approx -2\eta$ or, in terms of u_t,

$$\eta_t \approx -0.05 u_t d \tag{30}$$

(the usual approximation is $+\frac{1}{3} u_t d$.) A negative value for $\eta + \eta_t$ seems to be typical for convective flow fields and has been found previously for 2-D magneto-convection (cf. Brandenburg et al., 1989b). A positive magnetic diffusivity would describe a diffusion of magnetic flux. However, convection acts in the opposite way in that it concentrates magnetic flux.

We have reconsidered recently the determination of η_t imposing a gradient in $\langle \boldsymbol{B} \rangle$. Taking as boundary condition for example $B_y = B_0$ at the bottom and $B_y = 0$ at the top leads to a systematic electric current in the x-direction. The resulting turbulent magnetic diffusivity has then a *positive* extremum in the middle of the layer with $\max(\eta_t) \approx 10\eta$. This is in qualitative agreement with customary expections.

6. Conclusions

The present investigation has demonstrated that topological effects may be of great importance for MHD-convection. It is shown that, as a consequence of topological effects, anisotropies of the α-effect can play a dominant role. In particular the sign of α_V can be opposite to that expected from a first order smoothing approach. In addition, it seems that the usual approximations, $\alpha \approx \Omega d$ and $\eta_t \approx \frac{1}{3} u_t d$, could be seriously in error. The order of magnitude smaller values obtained for these coefficients found in the present investigations (although with the opposite sign), might well produce more realistic solar dynamo models.

It is interesting to note that Nicklaus and Stix (1988) have considered corrections to first order smoothing and found considerable modifications to previous results, in particular that the sign of the mean-field coefficients may change. In another context (topological pumping) Moffatt (1974) has pointed out that topological effects enter into the closure equations only for third order and higher correlation approximations.

It should be noted that even in the framework of first order smoothing the often quoted relation $\alpha = -\frac{1}{3} \tau \langle \boldsymbol{\omega}' \cdot \boldsymbol{u}' \rangle$ is only a crude evaluation of the correlation integral of $\boldsymbol{u}'$ and $\boldsymbol{\omega}'$ (cf. Krause and Rädler, 1980, Eq.(3.29)). One cannot exclude the

possibility that an exact evaluation of this integral may lead to a change of sign of α for certain types of turbulence.

However, a too close comparison between mean-field theory and simulations is at present not justified for a number of reasons. The presence of boundaries and flow patterns extending from top to bottom of the domain are not really in accordance with the picture of mean-field theory. It seems desirable to check whether our surprising results occur also for other field and flow constellations and for other boundary conditions, or whether it is just an artifact of the special model considered.

The magnetic Reynolds number achieved in the present 3-D simulations is around 40, which is close to, but still below, the critical value of about 60 for dynamo action found by Meneguzzi and Pouquet (1989). Thus, nearly twice the number of gridpoints may be needed to simulate convective dynamos. However, the possibility of dynamo action may depend on other things as well, for example on the magnetic boundary condition: Meneguzzi and Pouquet have employed a perfect conducting boundary whereas in our model a non-vanishing vertical magnetic flux is present from the beginning. Thus, an enhanced magnetic energy compared to the initial state (see Fig. 10) can just be a result of flux concentration rather than dynamo action. It is therefore impossible to detect dynamo action in our case.

The convection model considered here may perhaps not be well suited for modeling the lower part of the convection zone, because of the assumption of closed boundaries, and also because we have used enhanced molecular diffusivities rather than subgrid-scale diffusivities. The convective flux in our models is relatively small (at most 25%, cf. Tables 1 and 2. The convective flux would be much higher if, in the energy equation, the (enhanced molecular) diffusion of internal energy, e, was replaced by a (subgrid-scale) diffusion of entropy, s (cf. Chan and Sofia, 1986).

Applying our model to a layer above the base of the convection zone between 0.7 and 0.8 solar radii, we have, with $g \approx 1.5 \times 10^4 \mathrm{cm/s^2}$ and $d \lesssim 10^{10}\mathrm{cm}$, a sound travel time of about a quarter of an hour (cf. Sect 2.2). Thus, a time span of 500 sound travel times corresponds to about five days and the rotation period of our model would be about one day! Since the Taylor number for our model is 10^4 we have then a viscosity of about $10^{14}\mathrm{cm^2/s}$ and a mean magnetic field strength of nearly 200 kgauss. These are, of course, not appropriate conditions for the Sun: the rotation is too rapid, the viscosity too high, and the magnetic field too strong. On the other hand, we may also consider the solar rotation period of 25 days as the basic quantity. Compared to the Sun the speed of sound of the model is then 25 times too slow (or the gravity about 500 times too weak). A time span of 500 sound travel times corresponds then to about one hundred days, the viscosity is then $5 \times 10^{12}\mathrm{cm^2/s}$, and the mean magnetic field strength 10 kgauss.

Clearly, the real conditions at the base of the solar convection zone are impossible to simulate with present day computers. Although the rotation for our model is too rapid compared to the sound travel time, the rotation is in some sense also slow because there is, for example, no evidence for the flow being forced to be two dimensional (cf. Taylor-Proudman theorem). However, the most important quantity which should be comparable with the solar value is probably the ratio of rotation period and turnover time ($= 4\pi \mathrm{Ro} \approx 5$). This is not too far from the solar value of about unity. We feel that, in this sense, our model may really be of relevance for understanding convection at the bottom of the solar convection zone.

Although there are a number of limitations associated with the model, we hope that some progress in determining the α-effect for the Sun may be possible in the near future with the aid of direct simulations. There are, however, several important ingredients for the α-effect dynamo, which should be considered. For example, one could allow $\boldsymbol{\Omega}$ to be inclined with respect to $\boldsymbol{g}$. Effects of curvature may be important, necessitating an angle between $\boldsymbol{\Omega}$ and $\boldsymbol{g}$ that varies across the computational domain. Another problem is that of the boundary conditions, whose effect should be minimized. Instead of complicated penetrative boundary conditions one may confine the convective part between two stably stratified layers, similar to the computations of Hurlburt et al. (1986). Such techniques have been studied thoroughly in the non-magnetic case and it is tempting to apply them in the future to the MHD dynamo problem.

Acknowledgements. We would like to thank the members of the Potsdam dynamo group for many stimulating discussions on this topic, especially the referee of this paper, Prof. F. Krause. Dr. M. Steffen also suggested many improvements to the manuscript.

References

Brestenský, J., Rädler, K.-H.: 1989, *Geophys. Astrophys. Fluid Dyn.* **49**, 57

Brandenburg, A.: 1988, *Astron. Astrophys.* **203**, 154

Brandenburg, A., Tuominen, I.: 1988, *Adv. Space Sci.* **8**, (7)185

Brandenburg, A., Krause, F., Meinel, R., Moss, D., Tuominen, I.: 1989a, *Astron. Astrophys.* **213**, 411

Brandenburg, A., Pulkkinen, P., Tuominen, I., Nordlund, Å, Stein, R. F.: 1989b, in *Turbulence and Nonlinear Dynamics in MHD Flows*, eds. M. Meneguzzi, A. Pouquet and P. L. Sulem, Elsevier Science Publ. B.V. (North-Holland), p. 125

Brandenburg, A., Moss, D., Rüdiger, G., Tuominen, I.: 1989c, *Astron. Astrophys.* (submitted)

Chan, K. L., Sofia, S.: 1986, *Astrophys. J.* **307**, 222

Chandrasekhar, S.: 1961, Hydrodynamic and Hydromagnetic Stability, Oxford, Clarendon Press

Childress, S., Soward, A.: 1972, *Phys. Rev. Lett.* **29**, 837

Dziembowski, W. A., Goode, P. R., Libbrecht, K. G.: 1989, *Astrophys. J. (Letters)* **337**, L53

Eidson, T., M., Hussaini, M. Y., Zang, T. A.: 1986, in *Direct and Large Eddy Simulation of Turbulence*, U. Schumann and R. Friedrich (eds.), Notes on numerical fluid mechanics, Vieweg, Braunschweig - Wiesbaden, p. 188

Fautrelle, Y., Childress, C.: 1982, *Geophys. Astrophys. Fluid Dyn.* **22**, 235

Gilman, P. A., Miller, J.: 1981, *Astrophys. J. Suppl.* **46**, 211

Gilman, P. A.: 1983, *Astrophys. J. Suppl.* **53**, 243

Glatzmaier, G. A.: 1985, *Astrophys. J.* **291**, 300

Gough, D.O., Weiss, N.O.: 1976, *Monthly Notices Roy. Astron. Soc.* **176**, 589

Hurlburt, N.E., Toomre, J., Massaguer, J.M.: 1984, *Astrophys. J.* **282**, 557

Hurlburt, N.E., Toomre, J., Massaguer, J.M.: 1986, *Astrophys. J.* **311**, 563

Hurlburt, N.E., Toomre, J.,: 1988, *Astrophys. J.* **327**, 920

Jackson, J. D.: 1962, *Classical Electrodynamics*, New York

Kippenhahn, R.: 1963, *Astrophys. J.* **137**, 664

Krause, F.: 1967, Habilitationsschrift, University of Jena
Krause, F., Rädler, K.-H.: 1980, *Mean-Field Magnetohydrodynamics and Dynamo Theory*, Akademie-Verlag, Berlin
Krause, F., Meinel, R.: 1988, *Geophys. Astrophys. Fluid Dyn.* **43**, 95
Libbrecht, K.G.: 1988, in *Seismology of the Sun and Sun-like Stars*, ed. E. J. Rolfe, ESA SP-286, p. 131
Meneguzzi, M., Pouquet, A.: 1989, *J. Fluid Mech.* **205**, 297
Moffatt, H. K.: 1974, *J. Fluid Mech.* **65**, 41
Moffatt, H. K.: 1978, *Magnetic Field Generation in Electrically conducting fluids*, Cambridge University Press, Cambridge, p. 247
Nicklaus, B., Stix, M.: 1988, *Geophys. Astrophys. Fluid Dyn.* **43**, 149
Nordlund, Å. : 1985, *Solar Phys.* **100**, 209
Nordlund, Å., Stein, R.F.: 1989, in *Solar and Stellar Granulation*, eds. R. Rutten and G. Severino, Kluwer Acad. Publ.
Pouquet A., Patterson, G. S.: 1978, *J. Fluid Mech.* **85**, 305
Roberts, P.H.: 1988, *Geophys. Astrophys. Fluid Dyn.* **44**, 3
Rüdiger, G.: 1980, *Geophys. Astrophys. Fluid Dyn.* **16**, 239
Rüdiger, G.: 1989, *Differential rotation and Stellar Convection: Sun and solar-type stars*, Gordon & Breach, New York
Soward, A.: 1979, *J. Fluid Mech.* **90**, 669
Steenbeck, M., Krause, F., Rädler, K.-H.: 1966, *Z. Naturforsch.* **21a**, 369
Stein, R.F., Nordlund, Å.: 1989, *Astrophys. J. (Letters)* **342**, L95
Stein, R.F., Nordlund, Å., Kuhn, J.R.: 1989, in *Solar and Stellar Granulation*, eds. R. Rutten and G. Severino, Kluwer Acad. Publ., p. 381
Tuominen, I., Rüdiger, G.: 1989, *Astron. Astrophys.* **217**, 217

This article was processed by the author using Springer-Verlag TEX AA macro package 1989.